Available online at www.sciencedirect.com
ScienceDirect
Journal of the European Ceramic Society 30 (2010) 2505–2513
www.elsevier.com/locate/jeurceramsoc

Microstructural and chemical aspects of working-temperature aged Ca-doped CeO_2

M. Yan [a,*], T. Mori [a], J. Zou [b,c], G.J. Auchterlonie [c], J. Drennan [c]

[a] *Fuel Cell Materials Center, National Institute for Materials Science, Tsukuba, Ibaraki 305-0044, Japan*
[b] *School of Mechanical and Mining Engineering, The University of Queensland, Brisbane, QLD 4072, Australia*
[c] *Centre for Microscopy and Microanalysis, The University of Queensland, Brisbane, QLD 4072, Australia*

Received 14 January 2010; received in revised form 9 April 2010; accepted 23 April 2010
Available online 21 May 2010

Abstract

Aging behavior investigation can provide a necessary basis for evaluating the suitability of doped ceria as the electrolyte material for intermediate temperature solid oxide fuel cells under working circumstances. In the current study, the microstructural and chemical variations of Ca-doped CeO_2 with various aging conditions have been systematically investigated by means of transmission electron microscopy (TEM), electron energy-loss spectroscopy (EELS), X-ray photoemission spectroscopy (XPS) and X-ray diffractometry (XRD). TEM shows that crystal defects in terms of microdomain and superstructure are alleviated by the aging processing. Reduction of the tetravalent Ce can be induced by high temperature aging, and the reduction fraction has been quantitatively determined within a broad temperature range. A new cerium oxide phase with a crystal structure of primitive monoclinic ($a = 1.31 \pm 0.013$ nm, $b = 0.38 \pm 0.004$ nm, $c = 3.52 \pm 0.035$ nm, and $\beta = 94.7 \pm 0.3^\circ$) has been determined in the high temperature aged specimens. The possible effects of the evolutions in the microstructure and material chemistry on the ionic conductivity are discussed.

Keywords: Microstructure-final; Fuel cells; CeO_2; Aging

1. Introduction

For their potential to provide clean energy and to decrease the environmental impact caused by fossil fuels, solid oxide fuel cells (SOFCs) have drawn great attention in recent years.[1–4] With its economical advantage and being more environment-friendly compared with rare-earth doped CeO_2, Ca-doped CeO_2 has also demonstrated competitive ionic conductivity, promising as the electrolyte material for intermediate temperature SOFCs.[5–7]

Given the practical applications, electrolyte materials should operate at intermediate temperatures (generally between 300 °C and 700 °C) for extended periods. From this point of view, working-temperature aging study is an effective and critical pathway to develop reliable SOFCs. Previous studies on doped zirconia have suggested that long-term high temperature aging may lead to: (1) phase transformation towards phases with lower crystalline symmetry; (2) precipitation of long range ordered phases; (3) glassy phase segregation in the grain boundary; and (4) formation of short-range ordering.[8–10] Meanwhile, controversy still exists regarding to the resultant conductivity performance, with studies showing an increase[11] or a decrease[9] in the ionic conductivity. In fact, this means that the understanding of how aging affects the microstructural and chemical states of the electrolyte materials is still not satisfactory, because the conductivities of electrolytes are generally determined by a combination of their microstructural and chemical perspectives.

Compared with the extensive studies on doped zirconia, aging studies of rare-earth doped CeO_2 are limited to the works of Zhang et al.[12–14] They suggested that the effects of aging depend upon aging temperature and dopant concentration; unfortunately, it is far from adequate with respect to the microstructure affected by the aging processing. On the other hand, study of Ca-doped CeO_2 is lacking so far. To understand the aging behavior so as to provide optimal working conditions as well as to evaluate the thermal stability, a detailed analysis of Ca-doped CeO_2 is

* Corresponding author. Present address: School of Mechanical and Mining Engineering, The University of Queensland, Brisbane, QLD 4072, Australia.
E-mail address: m.yan2@uq.edu.au (M. Yan).

0955-2219/$ – see front matter © 2010 Elsevier Ltd. All rights reserved.
doi:10.1016/j.jeurceramsoc.2010.04.036

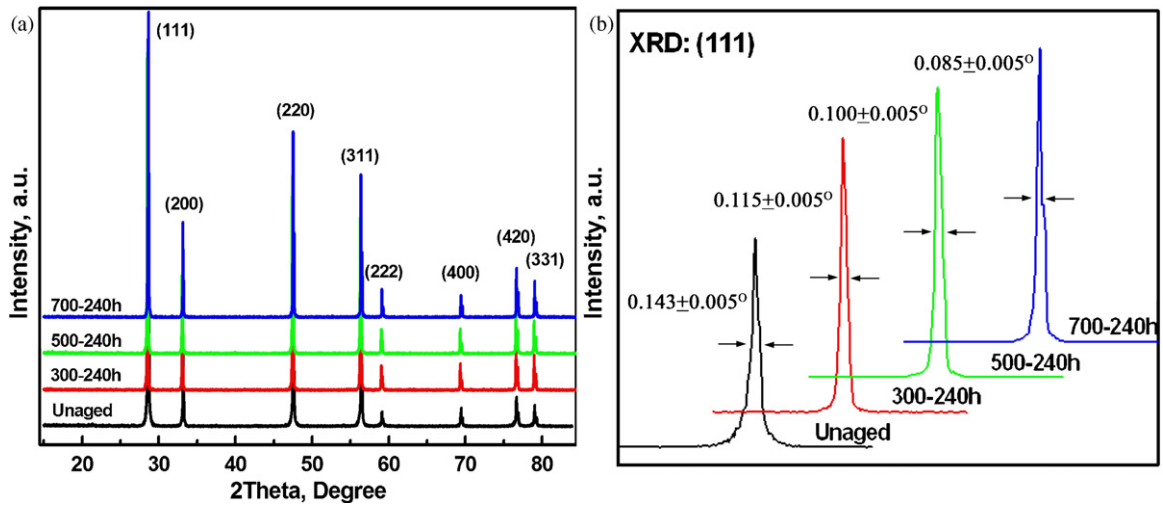

Fig. 1. XRD curves for the unaged and aged specimens: (a) full range patterns and (b) patterns within the range of (26.5–30.5°) with FWHM values presented.

required in terms of the microstructural and chemical evolution due to the aging processing.

In the current study, a Ca-doped CeO_2 ($Ca_{0.1}Ce_{0.9}O_{1.9}$) with various aging conditions was systematically investigated by means of TEM, XPS, EELS and XRD. The detailed microstructural and chemical variations due to the aging processing have been determined, and their potential influences on the ionic conductivity are discussed. A new cerium oxide phase has been identified during analyzing the high temperature aged specimens.

2. Experimental

2.1. Materials synthesis

The nanosized precursor powders of $Ca_{0.1}Ce_{0.9}O_{1.9}$ (in atomic percent, shortened as CDC hereafter) were prepared by a co-precipitation method; high-purity (>99.99%) cerium nitrate hexhydrate [$Ce(NO_3)_3{\cdot}6H_2O$], calcium nitrate tetrahydrate [$Ca(NO_3)_2{\cdot}4H_2O$] and ammonium carbonate[$(NH_4)_2CO_3$] were used.[5] The precursor powders were calcined at 850 °C for 2 h. Compacted pellets (under an isostatic cold pressure of ~15 MPa) were subsequently sintered at 1400 °C for 4 h. The heating rate for both the calcination and the sintering was set at 5 °C/min; the specimens were cooled to the room temperature within the furnace. Density measurement by the Archimedes method determined that the sintering density was no less than 95% of the theoretical density. Aging treatments were performed at 3 temperatures (300 °C, 500 °C and 700 °C), each with 3 different holding times (120 h, 240 h and 360 h). The heating rate was set at 10 °C/min and the specimens were naturally cooled. Hereafter, shortened terms, e.g. 500–120 h for a sample aged at 500 °C with a holding time of 120 h, will be used for the convenience of discussion.

2.2. Characterization

XPS was conducted on the PHI 5700 ESCA system using sintered pellets with a dimension of ~Φ3 mm in diameter and ~3 mm in thickness in a chamber pressure of (5–8) × 10^{-9} Torr. Pure CeO_2 was used as a reference in the XPS analysis, which was prepared by a method similar to that for CDC. A monochromatic Al K_α X-ray (1.4866 kV) was used as the incident radiation. The XPS samples were Ar-ion sputtered for ~1 min prior to the signal acquisition; the signal acquisition for each specimen normally finished within 3 min. Artificial signals due to the charge leakage were occasionally observable in some XPS specimens [such as the shoulder peak shown around 910 eV in Fig. 6(a)], and they were disregarded in the results analysis. The PC-ACCESS software was used to analyze the XPS spectra. Other details on the XPS experiments can be found in our recent publication.[15] XRD was performed at 40 kV/40 mA using a Cu K_α radiation (Rigaku RINT 2000HF Ultima).

TEM was performed on a JEOL NM-200 (operated at 200 kV) and a JEOL 300 (operated at 200 kV). Selected area electron diffraction (SAED) study was conducted on the former TEM, with an exposure time of ~50 s. The latter TEM is equipped with a Gatan Image Filter so that EELS can be performed. For EELS acquisition, the spectra were obtained with an energy dispersion of 0.2 eV/channel; the signal was usually collected within 3 min. The error tolerance in terms of the peak position was within ±2 eV based on experimental observations. The spectrum background was removed using the power law background subtraction, available in Digital Micrograph version 3.7.4.4.

3. Results

3.1. XRD results

XRD was employed to obtain general information on the microstructural variations induced by the aging processing. Fig. 1 shows the XRD results for the unaged CDC and several representative aged specimens, with Fig. 1(a) for the whole range patterns and Fig. 1(b) detailing the (1 1 1) peak in the range of (2θ: 26.5–30.5°). According to Fig. 1(a), the aged samples keep their crystal structure as a face centered cubic. Based on

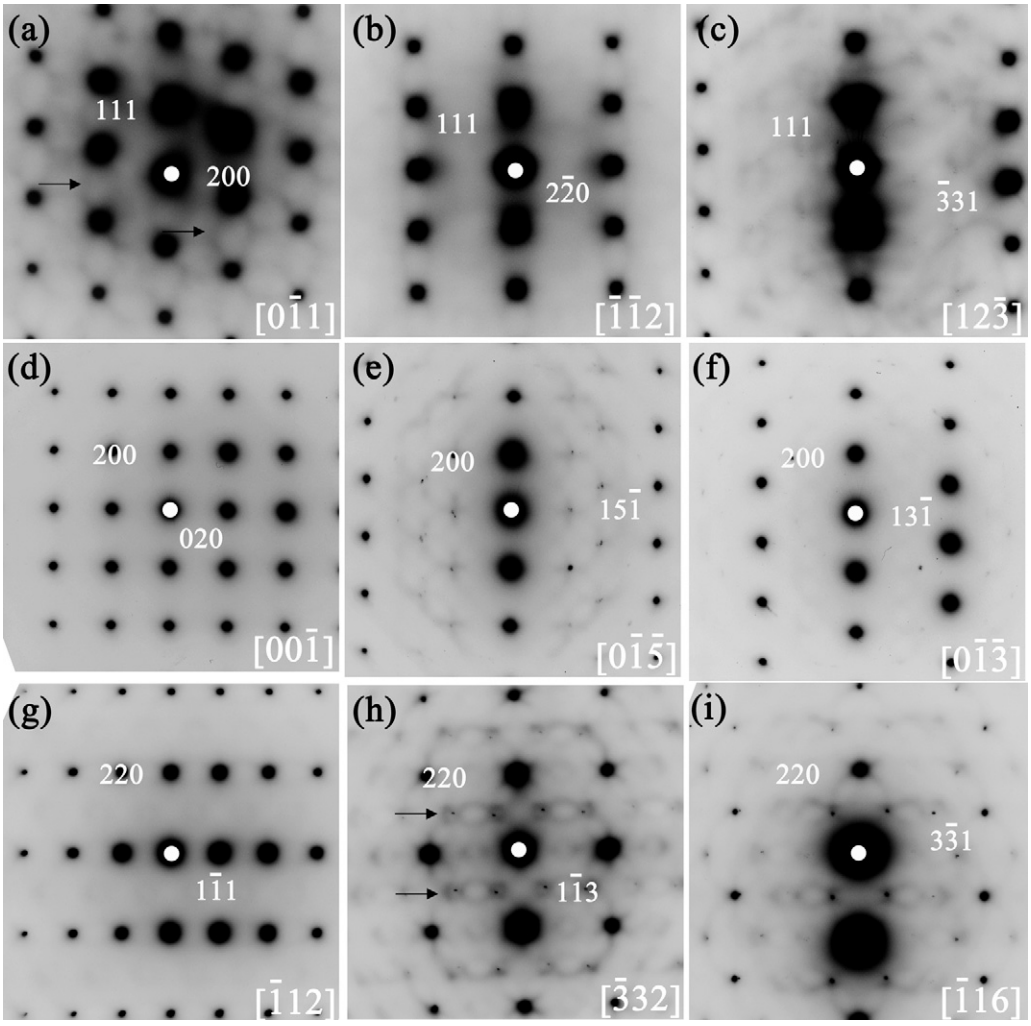

Fig. 2. TEM-SAED results for the unaged CDC, taken from major zone axes and with long exposure time. As typical examples, additional diffraction features are pointed out by arrows in (a) and (h).

Fig. 1(b), the values for the full width at half maximum (FWHM) of these spectra are measured, which present decreased FWHM with increasing the aging temperature (e.g. $0.143 \pm 0.005^\circ$ for the unaged and $0.085 \pm 0.005^\circ$ for the 700–240 h sample). According to the well-known Scherrer equation, an increased average grain size is expected ($d = 0.89\lambda/B\cos\theta$, where d is the grain size, λ is the XRD wavelength, θ is the diffraction angle and B is the FWHM value). In the meanwhile, an extended aging time does not lead to evident variations in the FWHM values (details not shown here), suggesting that the aging time is a less influential factor.

3.2. TEM analysis

In order to further understand the microstructural evolution induced by the aging processing, TEM was employed. Fig. 2 shows the selected area electron diffraction (SAED) results for the unaged CDC, where crystals were oriented along the atomically dense rows of {1 1 1}*, {2 0 0}* and {2 2 0}* and photographed with long exposure time [see Fig. 2(a)–(c), (d)–(f) and (g)–(i), respectively]. It is noticed that diffuse scatterings and even extra diffraction spots can be observed when tilting the sample to certain zone axes, such as the examples shown in Fig. 2(a) and (h).

To extend such analysis to the aged samples, SAED studies were conducted along the major zone axes as listed above, with typical results from two zone axes [{0 1 1}* and {2 3 3}*] shown in Fig. 3(a) and (b). By comparing the results that for the unaged and aged CDCs, it can be noted that both the diffuse scatterings and the additional diffraction spots become less prominent or even disappear with aging. Consistent with these SAED analyses, high resolution TEM (HRTEM) images for the aged samples, 700–360 h as an example, showed a nearly defect-free fine structure (see Fig. 4 for the details).

As a matter of fact, these fine SAED features, i.e. diffuse scattering and extra diffraction spot, are believed to be corresponding to crystal defects as microdomain and superstructure in doped CeO_2 materials; the variation in their diffraction intensity reflects the growth preference of these defects.[16,17] And it is generally accepted that lattice distortion, formed during doping (sintering) aliovalent elements into CeO_2, is responsible for the appearance of the superstructure[9]; the microdomain forms

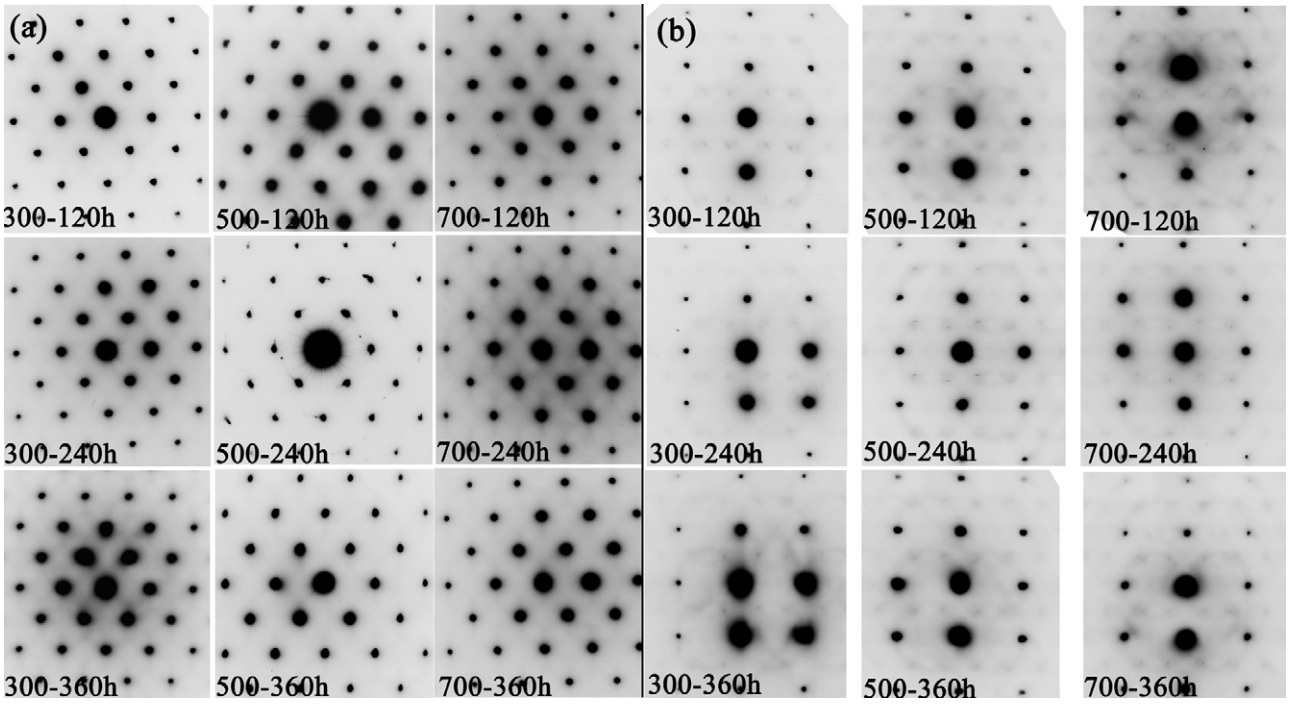

Fig. 3. TEM-SAED results for the aged CDCs: (a) [0 $\bar{1}$ 1] patterns and (b) [$\bar{2}$ 3 3] patterns.

as a kind of compensation to this lattice distortion.[18] With long-term aging like the processing in the current study, the lattice distortion in grains can be relaxed, consequently leading to the weakening of the superstructures as well as the microdomains.

During SAED analysis on the 700 °C aged samples, a new phase, although small in volume fraction, shows distinctive electron diffraction characteristics different from any known cerium oxides. Fig. 5 shows the analysis results, presenting a series of SAED patterns [Fig. 5(a)] that are obtained along the same dense row; the corresponding indexes are also shown in this figure. Based on these, the crystal structure of this phase can be determined as a primitive monoclinic with $a = 1.31 \pm 0.013$ nm, $b = 0.38 \pm 0.004$ nm, $c = 3.52 \pm 0.035$ nm, and $\beta = 94.7 \pm 0.3°$, with a unique b axis. Considering the reflection conditions, the possible space groups for this phase are $P2$, Pm, or $P2/m$.[19] Fig. 5(b) provides a bright field image for this phase and its composition is close to $Ce_{9.6}Ca_{35.6}O_{54.8}$ based on the energy-dispersive X-ray spectroscopy (EDX) result that shown in Fig. 5(c). With respect to the origin of this phase, there are two possibilities: (1) one is the segregation of Ca cations from the doped CeO_2 lattice to form this Ca-rich phase. In fact, similar phase transformation can be found in several doped zirconia systems by an aging processing[8,20]; (2) the other is as a crystallization product. In high temperature sintered CDC (such as 1400 °C as the current case), amorphous phases can be occasionally encountered and Fig. 5(d) shows a typical example from the unaged CDC (with the inset as a corresponding SAED pattern). This phase is enriched in Ca but free of Si. Observation of such amorphous phases is out of expectation to certain degree, but they were also suggested to exist by other studies; high temperature solid state reaction may be the reason for their formation.[21] From the free energy point of view, amorphous phases are metastable and can undergo phase transformation towards their equilibrium state (crystalline state) during the aging processing.[22]

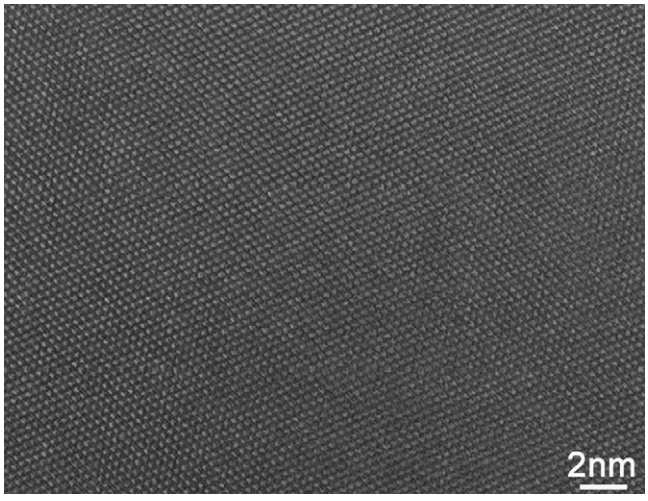

Fig. 4. HRTEM image for 700–360 h recorded at the zone axis of [0 $\bar{1}$ 1].

3.3. Chemical state of Ce

CeO_2 and doped CeO_2 materials are well known for their redox behavior, and very possibly a reduction will be induced as a result of the high temperature aging.[23,24] This change in the material chemistry will eventually affect the conductivity performance, for which XPS and EELS are employed to understand the details. It needs to mention that, in order to avoid the potential beam damage, all experiments were conducted with a time scheme as short as possible. In the meanwhile, the processing

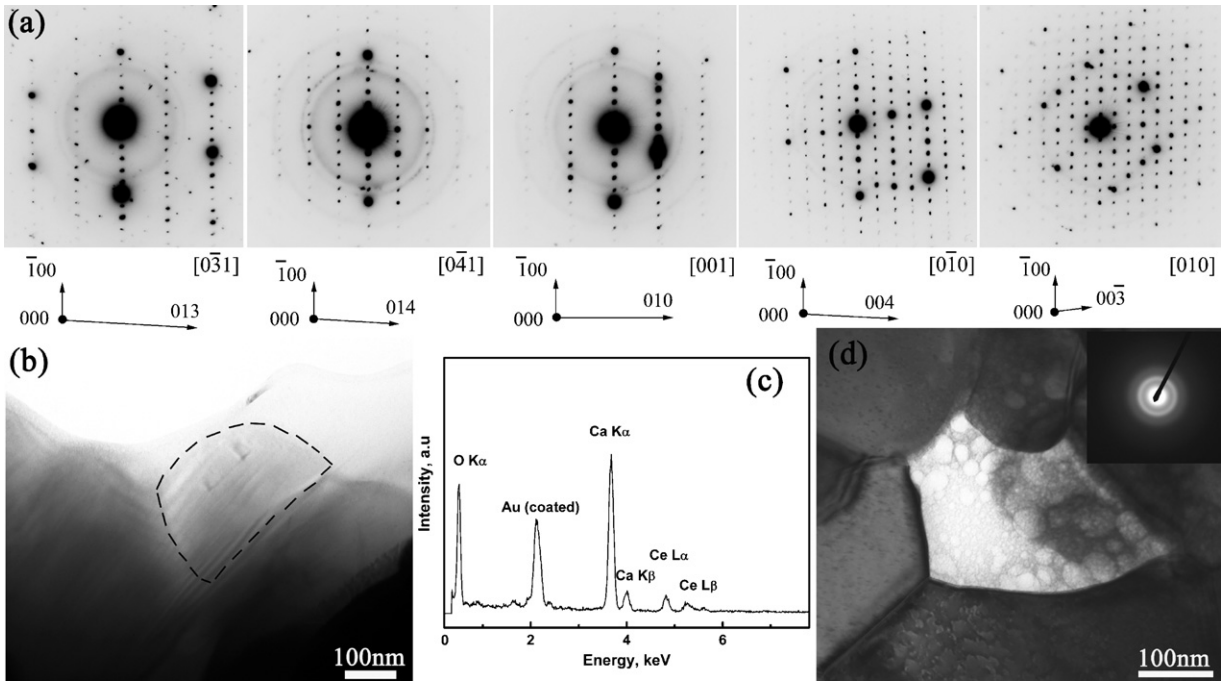

Fig. 5. TEM determination of the new phase: (a) a series of SAED patterns and the corresponding indexations, (b) a bright field image, (c) an EDX spectrum and (d) a bright field image for the amorphous phase, inset showing a corresponding SAED pattern.

pathways for all samples were identical, ensuring that their differences are only caused by natives of the materials rather than different experimental conditions.

Fig. 6(a) shows the XPS Ce 3d spectrum for undoped CeO_2, which is used as a reference as a 100% tetravalent Ce (Ce^{4+}) state. Furthermore, to quantitatively determine the reduction fraction, the spectrum of the undoped CeO_2 was deconvoluted using 11 components,[15] which fit well with the recorded spectrum as shown in Fig. 6(a). By performing similar analysis to the CDC specimens, the deconvolution results were determined and presented in Fig. 6(b) for the unaged CDC and in Fig. 6(c)–(h) for the aged CDCs. By comparing the binding energy of the deconvoluted components of the aged CDCs with those for the undoped CeO_2 (tolerance ± 0.4 eV), the fractions of Ce^{4+} in these states were calculated and the relevant results are presented in Table 1. It can be noted that both the aging temperature and the holding time have evident effects on the final chemical states: (1) high temperature aging induces noticeable reduction, with the higher the aging temperature, the lower the fraction of the remained Ce^{4+}. For example, it is calculated that the Ce^{4+} fraction in the 700–360 h sample is $76 \pm 5\%$ yet the fraction in the 500–360 h sample is $87 \pm 5\%$. In the meanwhile, no high level of reduction can be detected if the aging temperature is low, such as the cases for the samples aged at 300 °C; (2) extended aging time can cause enlarged reduction, except for the cases of the 300 °C aged specimens in which no evident reduction is observable. Relevant examples can be seen in 500–120 h ($95 \pm 5\%$) and 500–360 h ($87 \pm 5\%$).

To check the reliability of the XPS results, EELS was employed, as it is known that both the spectrum profiles of Ce $M_{4,5}$ edges and the ratio between Ce $M_{4,5}$ edges can be utilized as a basis for estimating the reduction.[16,25] Fig. 7 shows the EELS spectra presenting the Ce $M_{4,5}$ edges from the unaged CDC as well as several representative aged samples (300–240 h, 500–240 h, 700–240 h and 700–360 h). Based on this figure, two maxima, B and B′, are realizable for the unaged CDC, with two broader peaks denoted as Y and Y′. The former sharp peaks arise from quasiatomic, dipole-allowed transitions from an initial $3d^{10}4f^n$ to final states of the $3d^9 4f^{n+1}$ [25] and the latter two broader ones might originate from delocalization of the f-electrons (strong covalency hybridization between Ce 4f and O 2p states).[26] By comparing the profiles of the spectra for the unaged and the aged CDC, one can note that the EELS features for the lower temperatures aged samples, i.e. 300–240 h and 500–240 h, match closely to that for the unaged CDC. In contrast, the shoulder maxima (Y and Y') for the 700 °C aged

Table 1
Fractions of Ce^{4+} in the total Ce signals determined by means of XPS for the unaged and aged CDCs (error ±5%); ratio of the area fraction between EELS Ce $M_{4,5}$ edges is also listed (error ±0.004).

	Unaged	300–120 h	300–240 h	300–360 h	500–120 h	500–240 h	500–360 h	700–120 h	700–240 h	700–360 h
Ce^{4+} (%)	100	100	95	100	95	88	87	83	81	76
M_5/M_4	0.640	–	0.637	–	–	0.712	–	0.744	0.748	0.744
M_5/M_4 [22]	0.67 (Ce^{4+} = 100%); 0.72 (Ce^{4+} = 88%); 0.73 (Ce^{4+} = 79%); 0.75 (Ce^{4+} = 67%); 0.82 (Ce^{4+} = 39%)									

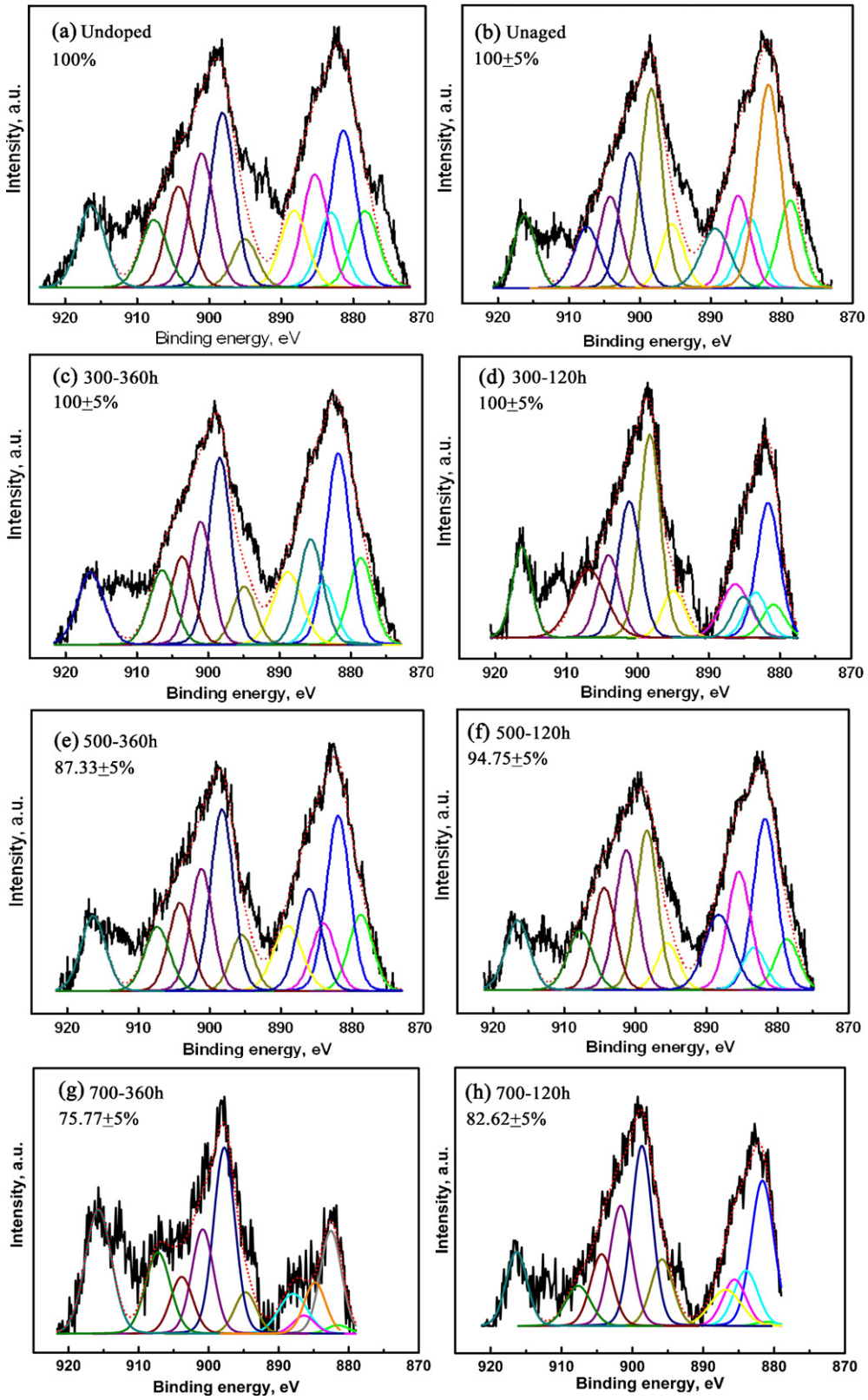

Fig. 6. XPS results for Ce 3d spectrum: (a) undoped CeO_2, (b) unaged CDC, (c) 300–360 h, (d) 300–120 h, (e) 500–360 h, (f) 500–120 h, (g) 700–360 h and (h) 700–120 h.

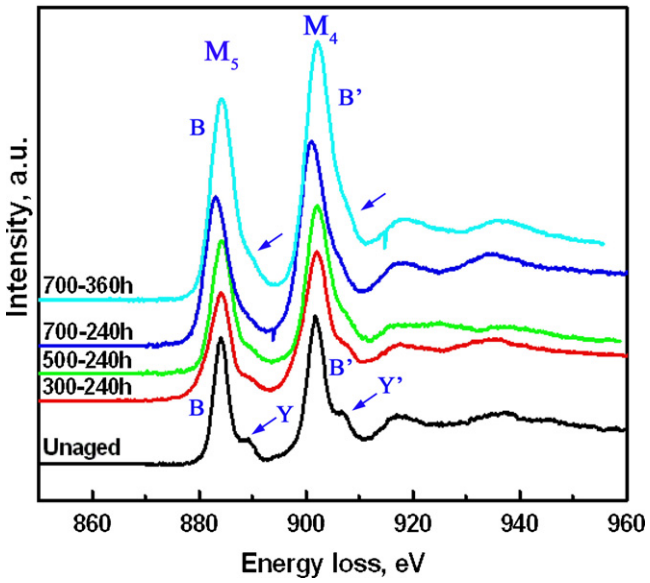

Fig. 7. EELS core level spectra for Ce $M_{4,5}$ edges for the unaged and aged CDC.

samples become less clear, representing a tendency towards the Ce trivalent state (Ce^{3+}) as evidenced by only two sharp maxima observable as its Ce $M_{4,5}$ edges.[25] In consequence, these EELS results indicate that a reduction has been induced due to the high temperature aging, confirming our previous XPS analysis. Moreover, no remarkable difference can be observed in terms of the peak positions, which were frequently affected by the slight drift of the zero loss peak during the signal acquisition; the similarity between the profiles of 700–240 h and 700–360 h suggests the aging time might be less influential than the aging temperature.

To quantitatively determine the reduction fraction, either the ratio of the area fraction[25] or the ratio of the peak intensity[16] between M_5 and M_4 edges were employed by researchers. In this study, we have found that the former is a better index, and the calculation results based on this method are listed in Table 1. Comparing our results with those from the reference, the 500–240 h ($R = 0.712$) sample should be close to a reduction level around 80% ($R = 0.72$ corresponding to a 79% of Ce^{4+} in Ref. [24]). This is basically comparable to the aforementioned XPS result ($88 \pm 5\%$ for 500–240 h). In the meantime, no clear difference in the M_5/M_4 ratio can be observed among 700 °C aged samples, which suggests this EELS index might be a less reliable method in terms of reduction calculation when compared with the XPS technique. In fact, the data from Ref. [25] also suggest this point, having a large variation in reduction (from 88% to 67%) within a very short range of R values (from $R = 0.72$ to 0.75).

3.4. Chemical states of Ca and O

Since the chemical state of Ce shows evident evolution with the aging processing, changes are also expected with the Ca and O elements. Fig. 8 presents the results for Ca obtained from both the EELS and the XPS studies, with the unaged CDC and the aged sample of 700–360 h as representative examples. As shown in Fig. 8(a), the EELS Ca L-edge spectrum for the unaged CDC shows a fine structure with approximately three separated peaks (main features are confined by arrows). In fact, the Ca L-edge is suggested to consist of four peaks in the case of Ca^{2+} in CaO, which could be assigned to $2p_{3/2}$-t_{2g}, $2p_{3/2}$-e_g, $2p_{1/2}$-t_{2g} and $2p_{1/2}$-e_g, respectively.[27,28] The probable reason for the observed three components in the present study is the merging of the third peak and the forth peak, reflecting a slightly different interaction environments between Ca^{2+} in CDC and Ca^{2+} in CaO in terms of core-hole spin–orbit splitting and crystal field. By comparison, the 700–360 h sample shows a single merged peak, largely different from the unaged CDC.

In terms of the O K-edge, the unaged CDC shows an EELS profile with three separated peaks [Fig. 8(b)] that is close to the situation for the pure CeO_2, having their originations from transitions to the p-like component of the hybrid Ce 4f and O 2p band (first peak) and unoccupied O 2p-like states (last two peaks), respectively.[29] In contrast, the aged sample shows a broadened spectrum, with the two lower energy peaks emerging into one shoulder peak. It is believed that reduced CeO_2 or Ce_2O_3 has this type of profile, with only two maxima realizable for the oxygen K-edge spectrum.[30]

Fig. 8(c) and (d) provides the XPS Ca 2p spectrum for the unaged CDC and 700–360 h. The corresponding O 1s spectra are shown in Fig. 8(e) and (f). For the unaged CDC, the low binding energy (LBE) pair dominates the Ca 2p spectrum, which originates from Ca^{2+} in doped ceria phases.[15] The high binding energy (HBE) pair is weak, implying that additional Ca^{2+} signal, if exists, might be present in the system with a small volume fraction. In comparison, the HBE pair greatly increases its fraction in the case of 700–360 h, which should originate from the reduced doped ceria. Similarly, the O 1s spectrum for the unaged specimen is fit well by two components, arising from the absorbed oxygen and O^{2-} in doped ceria phases respectively. If a third component can be deconvoluted, its fraction is fairly small, which has its contribution from O^{2-} in other phase(s) instead of doped ceria phases. This third signal, however, enlarges greatly in the aged 700–360 h, implying that it is contributed from the aging induced reduction. It needs to mention that, due to its small volume fraction, the XPS signal from the new cerium oxide phase is negligible and/or below the minimum detectability limit of XPS.

4. Discussion

Based on the aforementioned results, the following four consequences can be concluded for working-temperature aged CDC in terms of microstructural and chemical perspectives: (1) decreased amount/extent of crystal defects; (2) enlarged grain size with increasing aging temperature; (3) reduction from Ce^{4+} state towards Ce^{3+} state when the aging temperature is high and (4) formation of a new phase with a crystal structure of the primitive monoclinic.

Considering the resistances to the ionic conduction, it is acknowledged that: (a) the migration resistance within the grain interior (GI resistance, part of ΔH_m); (b) the migration resistance

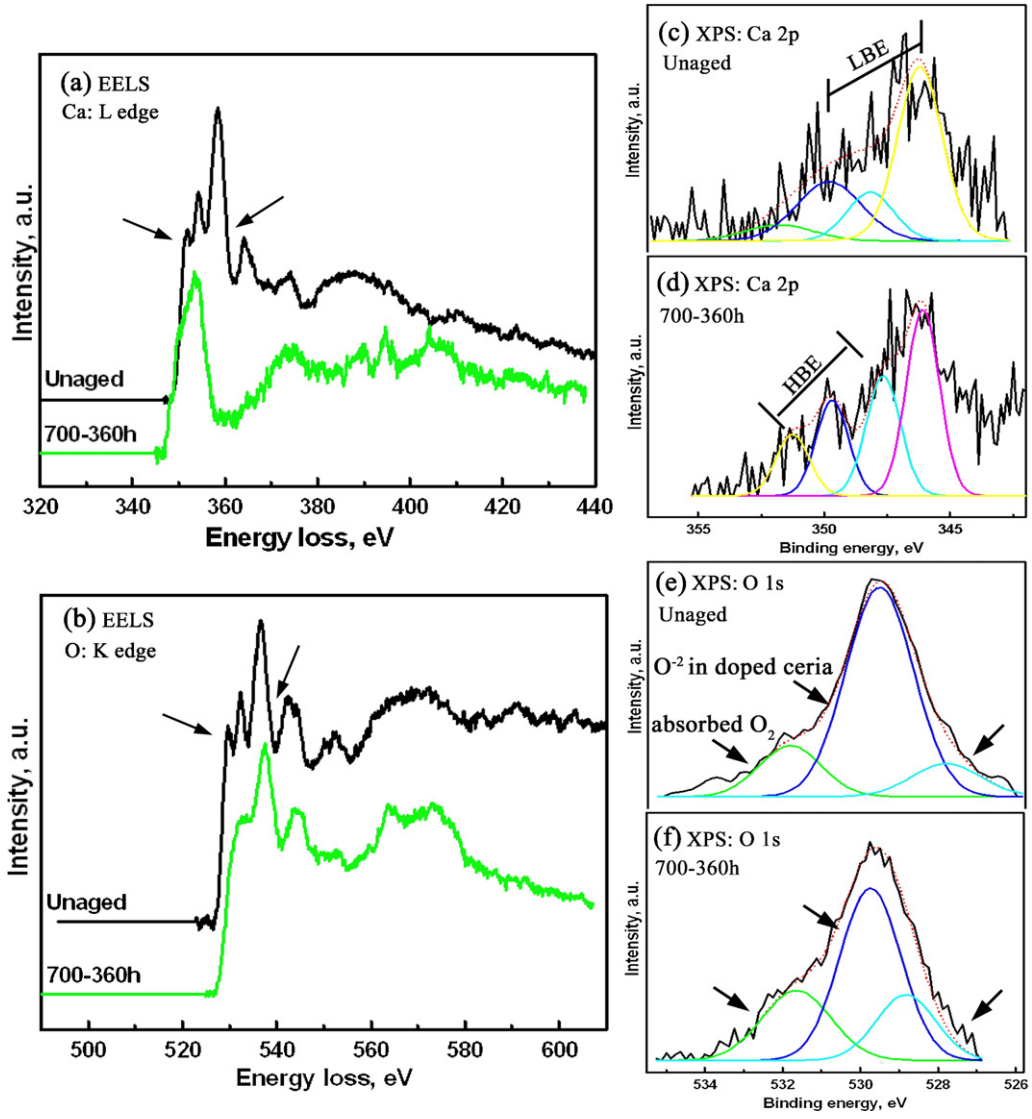

Fig. 8. EELS and XPS results for Ca and O in the unaged CDC and the aged sample of 700–360 h: (a) Ca L-edge, (b) O K-edge, (c) Ca 2p spectrum for the unaged sample, (d) Ca 2p spectrum for 700–360 h, (e) O 1s spectrum for the unaged sample and (f) O 1s spectrum for 700–360 h.

along the grain boundary (GB resistance, part of ΔH_m) and (c) the resistance from the complex defect association (defect association resistance, contributing to ΔH_A) will determine the final conductivity[31]:

$$\Delta H_a = \Delta H_m + \Delta H_A \quad (1)$$

where ΔH_a is the total activation energy, ΔH_m and ΔH_A are the migration enthalpy and association enthalpy of defects, respectively.

Consequently, the potential effects of aging on the conductivity can be discussed as follows: (a) the above mentioned factor (1) will decrease both ΔH_m and ΔH_A via the GI effect and the defect association effect, positively affecting the conductivity[15,32]; (b) the factor (2) will decrease the total amount of the grain boundary, implying a decreased GB resistance and positively contributing to the conductivity[33]; (c) since the factor (3) will decrease the amount of Ce^{4+} and also induce an electronic conductivity into CDC, the ionic conductivity will be decreased in the intermediate temperature region[2,3,31] and (d) the influence from the factor (4) is not very clear, because the ionic conductivity of the new phase cannot be clarified. In this aspect, literatures on doped zirconia suggest that phase transformation usually leads to a decreased conductivity.[8] Considering the new phase only shows in a very small volume fraction, the total impacts on the conductivity should remain small no matter how it affects.

Based on these discussions, we believe that the aging effects on the conductivity highly depend upon the aging temperature. High temperature aging may affect the conductivity negatively and yet aging at moderate temperatures (such as 300 °C) may contribute to the conductivity positively. In consequence, the appropriate working-temperature for CDC may need to avoid high temperatures such as 700 °C, which otherwise can undermine the microstructural and chemical stability and decrease the conductivity. Since the current study only focuses on the microstructual and chemical aspects of the aging processing,

it is hoped that there could be future studies with a focus on the conductivity. A combination of these studies will provide a comprehensive understanding of the aging behavior of Ca-doped CeO_2.

5. Conclusions

Through a systematic investigation on the aged Ca-doped CeO_2, the following conclusions can be made:

(1) The aging processing decreases the microstructural defects in terms of microdomains and superstructures, which exist in the high temperature sintered Ca-doped CeO_2.
(2) Tetravalent Ce will be reduced by high temperature aging; while low temperature aging will only lead to a mild or inconsequential reduction. Extended aging time will increase the reduction extent except for the case of low temperature aging where the phenomenon is not evident. The reduction fractions for different aging conditions have been quantitatively determined by means of XPS and EELS.
(3) The fine structure of EELS profile as well as XPS spectrum for Ca and O elements will be evidently affected by high temperature aging. Peak merging (for EELS) and developing of additional component (for XPS) can be realized for high temperature aged Ca-doped CeO_2.
(4) A new cerium oxide phase has been determined with the crystal structure of primitive monoclinic ($a = 1.31 \pm 0.013$ nm, $b = 0.38 \pm 0.004$ nm, $c = 3.52 \pm 0.035$ nm, and $\beta = 94.7 \pm 0.3^\circ$). The possible space groups for this phase are $P2$, Pm or $P2/m$, and its composition is close to $Ce_{9.6}Ca_{35.6}O_{54.8}$.

References

1. Dudek M. *J Eur Ceram Soc* 2008;**28**:965.
2. Steele BCH. *Solid State Ionics* 2000;**129**:95.
3. Fergus JW. *J Power Sources* 2006;**162**:30.
4. Esposito V, Traversa E. *J Am Ceram Soc* 2008;**91**:1037.
5. Yan M, Mori T, Ye F, Ou DR, Zou J, Drennan J. *J Eur Ceram Soc* 2008;**28**:2709.
6. Lu Z, Huang XQ, Liu W, He TM, Liu ZG, Liu J, et al. *J Rare Earths* 2002;**20**:47.
7. Yan M, Mori T, Zou J, Drennan J. *J Am Ceram Soc* 2009;**92**:2745.
8. Badwal SPS. *Solid State Ionics* 1992;**52**:23.
9. Kondoh J, Kikuchi S, Tomii Y, Ito Y. *Phys B: Condens Matter* 1999;**262**:177.
10. Moghadam FK, Yamashita T, Stevenson DA. In: Heuer AH, Hobbs LW, editors. *Science and technology of zirconia*, vol. 3. Columbus, OH: American Ceramic Society; 1981. p. 364.
11. Mori T, Drennan J, Lee JH, Li JG, Ikegami T. *Solid State Ionics* 2002;**154**:529.
12. Zhang TS, Ma J, Kong LB, Chan SH, Kilner JA. *Solid State Ionics* 2004;**170**:209.
13. Zhang TS, Ma J, Kong LB, Hing P, Chan SH, Kilner JA. *Electrochem Solid-State Lett* 2004;**7**:J13.
14. Zhang TS, Ma J, Huang HT, Hing P, Xia ZT, Chan SH, et al. *Solid State Sci* 2003;**5**:1505.
15. Yan M, Mori T, Zou J, Ye F, Ou DR, Drennan J. *Acta Mater* 2009;**57**:722.
16. Ou DR, Mori T, Ye F, Zou J, Auchterlonie G, Drennan J. *Phys Rev B* 2008;**77**:024108.
17. Allpress JG, Rossell HJ. *J Solid State Chem* 1975;**15**:68.
18. Mori T, Drennan J. *J Electroceram* 2006;**17**:749.
19. Hahn TH. *International tables for crystallography*. 5th ed. Dordrecht, The Netherlands: Kluwer Academic Publishers; 2002.
20. Badwal SPS, Ciacchi FT, Milosevic D. *Solid State Ionics* 2000;**136–137**:91.
21. Lopez Granados M, Gurbani A, Mariscal R, Fierro JLG. *J Catal* 2008;**256**:172.
22. Yan M, Zou J, Shen J. *Intermetallics* 2007;**15**:961.
23. Paparazzo E, Ingo GM. *J Electron Spectros Relat Phenomena* 1998;**95**:301.
24. Yeste MP, Hernandez JC, Bernal S, Blanco G, Calvino JJ, Perez-Omil JA, et al. *Chem Mater* 2006;**18**:2750.
25. Garvie LAJ, Buseck PR. *J Phys Chem Solids* 1999;**60**:1943.
26. Karnatak RC, Esteva JM, Dexpert H, Gasgnier M, Caro PE, Albert L. *Phys Rev B* 1987;**36**:1745.
27. Mkhoyan KA, Silcox J, Macuire MA, Disalvo FJ. *Philos Mag* 2006;**86**:2907.
28. Himpsel FJ, Karlsson UO, mclean AB, Terminello LJ, de Groot FMF, Abbate M, et al. *Phys Rev B* 1991;**43**:6899.
29. Arai S, Muto S, Murai J, Sasaki T, Ukyo Y, Kuroda K, et al. *Mater Trans* 2004;**45**:2951.
30. Garvie LAJ, Xu HF, Wang YF, Putnam RL. *J Phys Chem Solids* 2005;**66**:902.
31. Inaba H, Tagawa H. *Solid State Ionics* 1996;**83**:1.
32. Drennan J, Auchterlonie G. *Solid State Ionics* 2000;**134**:75.
33. Tschope A. *Solid State Ionics* 2001;**139**:267.